Hexagonal microtextured glass to achieve high optical performance in thin-film silicon solar cells

Padmakumar, Govind; Balaji, Aravind; Saitta, Federica; Perez-Rodriguez, Paula; van Swaaij, René A.C.M.M.; Smets, Arno H.M.

Important note

To cite this publication, please use the final published version (if applicable).
Please check the document version above.

Hexagonal microtextured glass to achieve high optical performance in thin-film silicon solar cells

Govind Padmakumar* , Aravind Balaji , Federica Saitta, Paula Perez-Rodriguez, René A.C.M.M. van Swaaij, Arno H.M. Smets

Photovoltaic Materials and Devices, Delft University of Technology, Mekelweg 4, Delft, 2628CD, Zuid Holland, the Netherlands

HIGHLIGHTS

- Periodic hexagonal micro-texture arrays on glass are successfully implemented for the first time in a superstrate configuration.
- With increased texture height and periodicity, light scattering at texture interfaces is enhanced.
- Hexagonal arrays facilitate conformal, crack-free growth of silicon crystals on glass.
- The short-circuit current of 28.60 mA/cm^2 is the highest reported for a single-junction nanocrystalline silicon solar cell without an anti-reflection coating.

ARTICLE INFO

ABSTRACT

Periodic hexagonal microtexture arrays (also known as honeycombs) are successfully implemented for the first time in a superstrate glass configuration. Hexagonal textures on glass demonstrate an anti-reflective effect when compared to flat glass. It is shown that light scattering increases at the honeycomb interfaces with an increase in texture height and periodicity. The performance of the textures is demonstrated using thin-film single-junction PV devices based on an indirect bandgap semiconductor material, nanocrystalline silicon (nc-Si:H), which requires light trapping in the infrared region of the spectrum. Inspecting the nc-Si:H bulk absorber suggests a conformal, crack-free growth of crystals on the hexagonal arrays. Short-circuit current density (J_{SC}) increases with an increase in the aspect ratio of the superstrate, without compromising voltage and fill factor. The J_{SC} enhancement is attributed to a combined benefit of (i) the anti-reflective nature of developed textures, (ii) trapping light within the absorbing layer through multiple order diffraction at the front and (iii) reflection from a back reflector with adapted hexagonal morphology. With the above observations, a J_{SC} of 28.6 mA/cm^2 (photovoltaic conversion efficiency of 9.3 %) is achieved for a 5 μm periodic texture with a height of 1 μm (aspect ratio = 0.21). This is the highest reported J_{SC} for a single-junction nc-Si:H solar cell in a superstrate configuration without an external anti-reflection coating.

1. Introduction

For thin-film solar cell technologies, such as copper indium gallium selenide, cadmium telluride, amorphous silicon, nano-crystalline silicon and perovskite, minimising absorber-layer thickness offers multiple benefits, including high production throughput, lower production costs, improved stability against light-induced degradation and enhanced carrier collection. To achieve high efficiency with thin layers, these photovoltaic (PV) devices require enhanced optical performance, which is accomplished by increasing light trapping [1]. This is typically achieved using random or periodic textures that scatter light at the interfaces. This extends the light path length, thereby improving photoconversion efficiencies [1–5]. Random textures have been extensively explored and correlated with enhanced optical performance [6–9]. In recent years, periodically textured substrates have been extensively studied as an alternative route and have been reported to achieve current densities higher than those conventionally used with randomly distributed textures [10–15].

Typically employed periodic textures are either pyramidal in shape or two-dimensional (2-D) gratings. However, thin-film PV technologies with a crystalline phase in the absorber are not compatible with the

---

steep slopes of the pyramidal shape [7,16,17]. In contrast, a 2-D grating shape facilitates high-quality crystal growth [16]. The periodic shape that can cover an area with the least perimeter is a hexagon [18]. For crystal depositions, hexagon-shaped textures (also known as honeycomb (HC) textures) minimise the length of sharp boundaries created by texture borders, thereby reducing defect formation [19]. Different methods to make hexagonal-shaped periodic textures on potential solar cell substrates include nanoimprint lithography [20,21], laser ablation (for sheet metals) [22,23], or photolithography [19,24,25]. HC textures have been previously implemented in monocrystalline silicon solar cells [4,26], as well as in thin-film solar cell technologies [20,27]. In wafer-based technology, HC textures are implemented on the illuminated side of wafer substrates [3,4,26]. In thin-film technology, hexagonal periodic arrays are typically employed on opaque substrates on the reflective side [19,27–30]. The photoactive layers are subsequently deposited on these arrays. In such cases, the morphology features flatten out when multiple layers are stacked on top of it. This means that the morphology of the illuminated cell surface is not a replica of the hexagons [31] and fails to capitalise on the full light-management potential of texture. On the contrary, superstrate configuration enables us to implement textures on the illumination side of a solar cell, typically on transparent superstrates [6,32]. Thus, the initial light scattering before entering the photoactive layers in the superstrate configuration is independent of layer conformality. A feasible method for creating HC textures on glass is to use photolithography [33,34]. The optical properties of hexagonal textures on glass and their implementation in superstrate-configuration solar cells have not been extensively explored yet and are the primary focus of this article.

For the first time, this article presents a comprehensive optical characterisation of hexagonal microsized textures on glass. The optical interaction is correlated with the physical height and surface features of the hexagons. Finally, we explore the effect of periodic front-textured glass on solar cell performance. The HC-textured glass is utilised as a superstrate for an indirect bandgap material, such as hydrogenated nanocrystalline silicon (nc-Si:H), to fabricate single-junction solar cells. Additionally, we examine the quality of silicon crystal growth on the texture.

2. Materials and methods

2.1. Generating hexagonal textures on glass

This study uses Corning glass XG boro-aluminosilicate glass wafers, with a 4-inch diameter and 0.7 mm thickness, featuring a primary flat side [35,36]. UV photolithography is used to generate HC textures on the glass superstrates. A flowchart of this approach is presented in Fig. 1. In Step 1, the Corning glass wafer is cleaned with 69.5 % HNO_3 for 3 minutes. The wafer is dried and annealed in Step 2 at 110 ° for 10 minutes (pre-coating bake). In the subsequent step, the wafer is exposed to hexamethyldisilazane (HMDS) for 150 s at 150 ° C, using nitrogen as the carrier gas. In Step 4, 2.1 µm of Shipley SPR3012 positive photoresist is spin-coated. An extra annealing (post-coating bake) is then performed at 100 ° for 90 s. In Step 6, UV exposure is conducted using a chromium reticle with periodically distributed holes. The periodicity (P) of hexagonal textures is directly determined by the orifice periodicity of photoresist masks produced by UV lithography. Step 7 involves pattern development, in which the exposed areas of the photoresist are removed. The photolithography technique implemented on glass requires an additional hard-bake (Step 8 - post-development bake) at 140° C for 30 minutes. In Step 9, the pattern is transferred from the mask to the Corning glass wafer through a 20-minute dip in premade buffered hydrofluoric acid (BHF), comprised of ammonium fluoride (NH_4F) (40 %): hydrofluoric acid (HF) (49 %) in a ratio of 7:1. The wafer is then rinsed with deionised (DI) water, and the remaining photoresist is removed. The processing parameters in the flowchart shown are optimised so that the etched hexagonal shapes beneath the photoresist mask are well-defined and not over-etched. The detailed concepts and optimisation of

the steps involved in creating hexagonal textures on glass are discussed elsewhere [33]. An image of these HC textures obtained by Atomic Force Microscopy (AFM) is given in Fig. 2.

For the physical and optical characterisation of HC in this study, 75 different hexagonal microtextured glass wafers were fabricated. Each sample has a surface that is geometrically different from the others. This ensures an extensive sample set of hexagonal patterns on glass, which has not been attempted in the literature. Of the 75 glass wafers, 61 samples exhibit a periodicity of 3 µm, with heights ranging from 150 nm to 521 nm. Seven samples were created with periodicities of 4 µm and 5 µm, having height ranges of 590 nm to 748 nm and 802 nm to 1012 nm, respectively. The sample with the maximum attained height for 3 µm, 4 µm and 5 µm periodicity is named HP3, HP4 and HP5, respectively.

2.2. Physical characterisation of hexagonal microtextures

AFM maps the surface morphology of HC textures using a Bruker AFM FastScan in FastScan closed-loop scanner head mode. Scanning areas of 16 µm × 16 µm are used. Extraction of feature heights from AFM images was conducted using NanoScope Analysis (version 2.0) software from Bruker. The distribution of angles subtended by surface vectors with respect to the vertical plane is used as a metric to analyse surface angles (θ_s) in Gwyddion (version 2.63). The 2D power spectral density (PSD) plot is a quantitative measure of surface features. PSD is a spatial frequency representation of the morphology based on the discrete 2-dimensional Fourier transform of the height-height correlation function [37–39].

After the deposition of the front electrode IOH, the sheet resistance ($R_{sheet,IOH}$) is determined using the four-point probe (4PP) method. This measurement is carried out at 23 ° with an AIT CMT-SR2000N system, which uses four contacts arranged linearly and equidistantly with a 1 mm gap.

2.3. Transmission characterisation of hexagonal microtextures

For measuring transmission, all glass samples were probed with light on the flat side, as shown in Fig. 3(a). The LAMBDA 1050+ UV/Vis/NIR spectrophotometer, equipped with a 150 mm InGaAs integrating sphere from PerkinElmer, was used to record the optical transmission. This measurement was performed over a wavelength (λ) range of 300 to 1200 nm in 10 nm increments. The total transmission (T_{TOT}) was measured as a percentage ratio of transmitted light to total incident light. The diffused transmittance (T_D) was measured as a percentage ratio of the non-specular component of light to the total transmitted light.

2.4. Angular intensity distribution (AID) measurement of hexagonal microtextures

A wafer with periodic hexagonal microtextures exhibits diffractive patterns under white light. Fig. 3(B) shows a textured wafer under a TL lamp viewed with bare eyes. To determine the extent of angular scattering of the HC textures, the AID of transmitted light was recorded using the 180 mm automated reflectance/transmittance analyser (ARTA) accessory on a LAMBDA 950 PerkinElmer unit. A schematic diagram of the setup is shown in Fig. 4(A). Measurement details of AID for transparent objects can be found elsewhere [32,40]. The ARTA detector moves in a cylindrical plane with the sample at the centre. The sample is positioned in a plane perpendicular to the direction of the incoming light ray. The motion of the detector is shown in Fig. 4(A). The AID measurement was performed over a λ range of 300 nm to 1000 nm. The AID is measured in transmission mode, and the angle values range from 0 to 90°, where the angles indicate the position of the detector with respect to the surface normal of the sample. It is to be noted that only a quarter of the transmission sphere is required, as the AID curve is symmetric.

When analysing the results of the ARTA tool, it was assumed that a texture serves as a random scatterer, which challenges the measurement
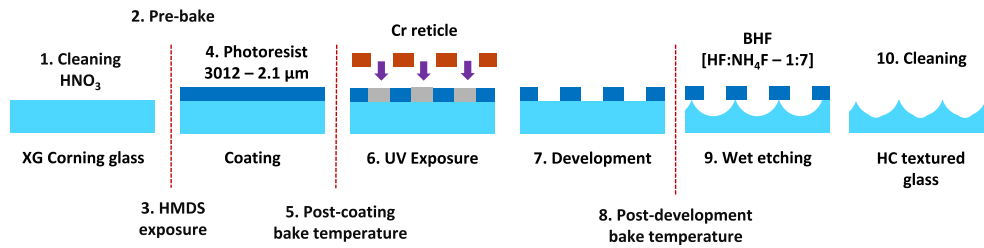
Fig. 1. Process flow for generating hexagonal microtextures (HC) using UV photolithography on Corning glass superstrates.
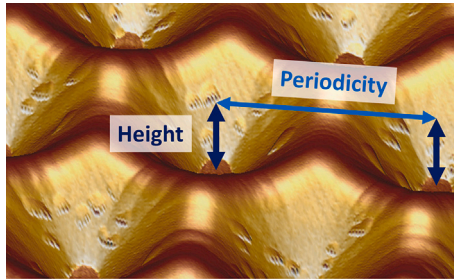

Fig. 2. AFM image of hexagonal micortextures developed on glass. Height and periodicity of the textures are also demonstrated. Other significant dimensions related to hexagons are given in the Supplementary Fig. 2.
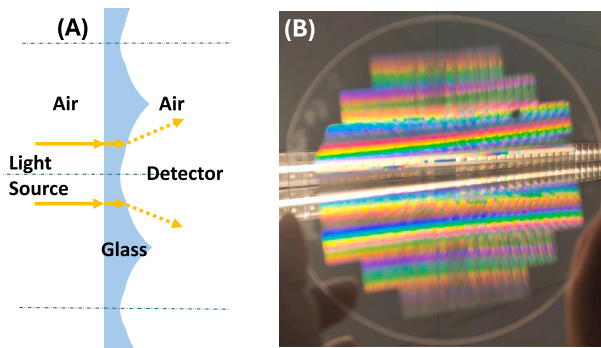

Fig. 3. (A) Orientation of textured wafers with respect to the light source and detector for optical measurement. (B) A wafer with hexagonal microstructures viewed under a tube-luminescent lamp. The 2D hexagonal periodicity of the hole positions drives the rainbow effect.

of 2D surface gratings that exhibit multiple diffraction peaks in a 2D plane. Fig. 4(B) is the photograph of the far-field pattern (in transmission mode) generated by the HC textured wafer when probed with a 635 nm laser on a plane parallel to the wafer. The six-fold symmetrical texture of the sample yields a pattern featuring first, second, third, up to an nth order spots, as illustrated. To account for light spots, which are otherwise located at an angle to the horizontal plane in the measurements, the wafer is rotated at 172 rotations per minute (rpm) about its vertical axis. This rotation, in turn, converts all the light spots into rings representing the maxima and minima of the patterns, as shown in Fig. 4(C). In this approach, light ring intensities are incident on the detector over a sufficient time and the values are recorded.

2.5. Fabrication of solar cells

The optical characterisation conducted on the texture is in an air/glass/air system, where the incident light ray at the glass/air interface has a higher-to-lower refractive index variation. A solar cell has an air/glass/silicon/back-reflector system, where the incident light

ray at the glass/silicon interface has a lower-to-higher refractive index variation. This difference makes the study on the air/glass/air system not one-to-one translatable to solar cells. Therefore, to evaluate the potential of textured interfaces, multiple solar cells are fabricated with the following specifications on different texture heights and periodicities.

The solar cell architecture employed in this study is shown in Fig. 5. Solar cells were fabricated on hexagonal-textured wafers with periodicities of 3 μm, 4 μm, and 5 μm. Single-junction nc-Si:H solar cells were fabricated in a superstrate configuration. The solar cells have hydrogenated indium oxide (IOH) as the front transparent conductive oxide (TCO). IOH is RF magnetron sputtered from a ceramic indium oxide (In_2O_3) target in $Ar/O_2/H_2O$ mixtures. The trace of water vapour suppresses crystal growth of IOH, which results in the deposition of amorphous IOH [41,42]. A 150-nm thick IOH layer has $R_{sheet,IOH} = 21 \pm 0.7$ Ω/sq. The silicon alloy deposition was done in a plasma-enhanced chemical vapour deposition (PECVD) multi-chamber tool with dedicated processing chambers for the boron-doped hydrogenated nanocrystalline silicon oxide p-layer (B-doped (p)nc-SiO$_x$:H), intrinsic hydrogenated nanocrystalline silicon ((i)nc-Si:H) and phosphorus-doped hydrogenated nanocrystalline silicon oxide n-layer (P-doped (n)nc-SiO$_x$:H). The B-doped nc-SiO$_x$:H layer (16 nm thick) and P-doped nc-SiO$_x$:H n-layer (20 nm thick) were deposited using radiofrequency (13.8 MHz) in the PECVD tool at 180 ° C substrate temperature and using B_2H_6 and PH_3 as dopant gases, respectively. The (i)nc-Si:H absorber layer was deposited at very high frequency (40.68 MHz) at a deposition rate of 0.49 Å/s at 170 ° C substrate temperature. In PECVD processing, the deposition rate on textured surfaces is lower than on flat glass. This deposition rate scales down by a factor equivalent to the effective surface area change due to texturing [43]. Based on this value, the deposition rates of all layers for the solar cells mentioned are adjusted to achieve similar layer thickness across different textures. The solar cells have a back reflector consisting of i-ZnO (60 nm) sputtered at a substrate temperature of 200 ° C and an evaporated silver (300 nm) layer. i-ZnO acts as a suppressor for the surface plasmon resonance at the silver-silicon layer interface [44]. The front contact is a 500 nm thick aluminium layer, and the back contact comprises chromium (30 nm) and aluminium (500 nm). The solar cell area is defined by 5 mm × 5 mm squares. This results in a solar cell structure of IOH (150 nm)/(p)nc-SiO:H (16 nm)/(i)nc-Si:H (3200 nm)/(n)nc-SiO:H (20 nm)/i-ZnO (60 nm)/Ag (300 nm) for single junction solar cells. No anti-reflective coating was used at the front of any of the solar cells presented in this study.

2.6. Characterisation of solar cells

The solar cells are characterised by their current density-voltage (J-V) performance and external quantum efficiency (EQE). J-V measurements are conducted at 25 ° using a WACOM-class AAA xenon-halogen dual-lamp continuous solar simulator, mimicking AM1.5G illumination (100 mW/cm^2). EQE is measured using an in-house-developed tool with monochromatic light. EQE measurements are performed at a short-circuit condition of 0 V and at a reverse bias condition of -2 V in some cases. Short-circuit current density (J_{SC}) is calculated by integrating the EQE measurements of solar cells against the AM1.5G spectrum, denoted
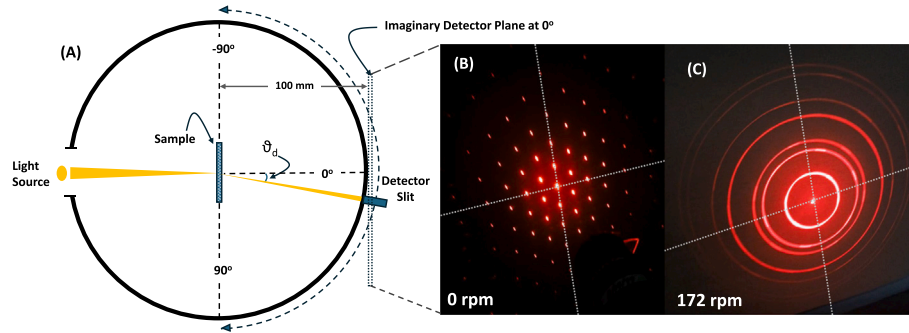
Fig. 4. (A) Top view of ARTA accessory on a LAMBDA 950 PerkinElmer unit. The direction of the sweep, the sample position, and the light ray are depicted in the picture. (B) Far-field diffraction pattern of hexagonal microtextures interacting with a 635 nm laser. The hexagonal array of diffraction orders mirrors the symmetry of the surface craters. (C) The pattern in (B) was transformed into circles at a rotation speed of 172 rpm.
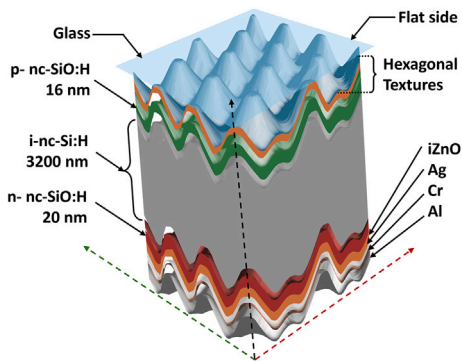

Fig. 5. Cell architecture and layers of an nc-Si:H single-junction solar cell.

$J_{sc,EQE}$ henceforth. This helps to prevent the overestimation or underestimation of current caused by any mismatch between the solar spectrum and the WACOM solar simulator. This approach also eliminates errors in estimating the active cell area in small-area solar cells. The total absorptance of the solar cell $(1 - R)$ is derived from reflectance (R), which is also recorded using a UV/Vis/NIR spectrophotometer. A Renishaw in-Via Raman microscope is used to determine the crystallinity (χ_c) of the nc-Si:H absorber with a 633 nm red laser. In addition, scanning electron microscopy (SEM) with a Hitachi Regulus 8230 at an acceleration voltage of 1.5 kV is used to create cross-sectional images of solar cells on glass.

3. Results and discussion

3.1. Surface profile of hexagonal craters

An isometric view of the hexagonal textures on a Corning glass wafer, along with its characteristic dimensions, is given in Fig. 6(A). The two axes, named the R-axis and G-axis, represent the innate 30° asymmetry of the surface morphology in HC. AFM images of HP3, HP4 and HP5 are shown in Fig. 6(B), (D) and (F) respectively and the corresponding extracted surface profile data are given in Fig. 6(C), (E) and (G). The observed nature of craters is typically spherical, with no flat bases. We observe that, for a fully developed hexagonal pattern on a glass superstrate, the maximum height along the R-axis (referred to as H_r henceforth) and the maximum height in the G-axis (referred to as H_g henceforth) are different. We consider H_r as the characteristic height of the texture and define the aspect ratio (AR) as H_r/P as conventionally used in the literature [3,13,25,31,45]. For the same processing conditions, all three parameters — H_r, H_g and AR — increase with HC periodicity. An inverted conical protrusion, with a saddle point, is present at the intersection point of three hexagons. Each saddle point is

located at a distance of $P/2$ from the adjacent saddle points. The R-axis is chosen so that the saddle points (and conical features) are positioned along this axis. The height difference between the two axes, $H_r - H_g$, represents the height of the saddle. This idea of $H_r - H_g$ is illustrated in Fig. 6(C), (E) and (G).

The summary of all height parameters shown in these images is presented in Table 1. H_r, $H_r - H_g$ and AR increase with an increase in periodicity. For the cross-section profiles along the G and R axes, the surface profiles can be fitted with good agreement to fragments of circles. These circles and the corresponding radii of the fitted spheres are shown in Supplementary Fig. 5 of this paper. In total, four significant height features are present in the hexagonal textures, in descending order: P, H_r, H_g, and $H_r - H_g$.

3.1.1. Slope distribution of the craters

The occurrence distribution of θ_s for HP3, HP4 and HP5 is recorded in Fig. 7. For each sample, three sets of angles can be identified as follows. Set 1: angles < 3° marking the inflection points on the texture morphology. This includes crater boundaries, the saddle points and the bottom flatness of the hexagons. Set 2: angles between 5° and 15°. This region represents the neighbourhood of the inflection regions. Set 3: angles > 15° represent the walls of the hexagonal surface. This set of angles determines the tapering angle of the hexagonal grating. Set 3 has the highest contribution to the total θ_s in all three samples.

An overall trend is observable for all three sets. For HP3, the peak in angle Set 1 indicates that the flat regions are more pronounced in HP3 than in HP4 and HP5. HP3 has broader boundaries and flatter bases. Sets 2 and 3 show a shift of the peak towards smaller angles with increasing periodicity, indicating that the crater walls become less steep as the periodicity increases. This is an interesting observation, considering that the texture height follows the order HP5 > HP4 > HP3. Furthermore, this observation implies that higher periodicity in hexagonal craters results in deeper textures and decreased steepness. For Set 3, HP5 has a concentrated peak occurrence when compared to HP3 and HP4, indicating a uniform taper for HP5 craters.

3.1.2. Micro-scale and nano-scale features

PSD analysis of the HP3, HP4 and HP5 surfaces is presented in Fig. 8. The PSD of a texture at low frequencies (Zone 1) indicates the presence of features with large lateral and vertical dimensions. The high-frequency zone (Zone 2) represents small features in the texture. Beyond Zone 2 is the decay zone where the fractal nature and noise come into effect [37, 39]. In Zone 1, the highest value of PSD occurs for HP5, followed by HP4 and HP3 at their respective P^{-1} values. The periodicity of the textures determines the most prominent features in the sample. The high PSD values in Zone 1 are indicative of the height H_r. The highlighted Zone 2 includes the spatial frequency of saddle points $(2P^{-1})$ in the morphology. In this high-frequency zone, HP5 shows more small-scale features than HP4 and HP3.
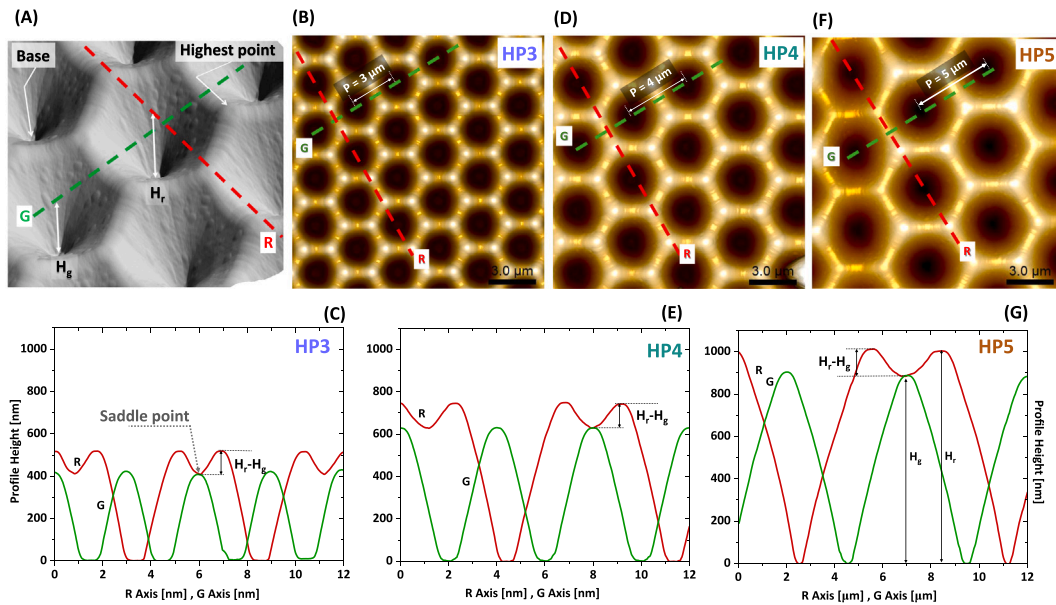
Fig. 6. AFM data visualised for hexagonal microtextures on glass. The 30° asymmetrical directions are highlighted by two lines, namely the R-axis and the G-axis. (A) The isometric view of HC. The highest point of the texture, the base of the crater and two defined axes, the R-axis and G-axis, are illustrated. Top view of (B) HP3 and (C) the corresponding R and G axes profiles (D) HP4 and (E) the corresponding R and G axes profiles, (F) HP5 and (G) the corresponding R and G axes profiles.

Table 1
Height and area parameters of the hexagonal textures.

Superstrate	P [μm]	H_r [nm]	H_g [nm]	$H_r - H_g$ [nm]	AR [%]	Surface Area (of 16 μm × 16 μm projected area) [μm^2]
HP3	3	521	412	109	17.3	272.7
HP4	4	748	628	120	18.8	270.9
HP5	5	1012	865	147	20.2	267.8

3.2. Optical interaction of hexagonal textures

3.2.1. Hexagonal textures in transmission

Fig. 9 plots the T_D values in % versus H_r at λ of 300 nm, 400 nm, 600 nm, 800 nm, 1000 nm and 1200 nm for 21 samples (7 samples each for periodicities 3 μm, 4 μm and 5 μm) with well-developed hexagonal shapes. The lines serve as guides for the eye to identify the effect of H_r and periodicity on T_D in Fig. 9. The change in T_D is almost negligible for $\lambda = 300$ nm. For $\lambda = 400$ nm, T_D saturates at around 85 %. As H_r and periodicity increase, the T_D increases linearly for all $\lambda > 600$ nm. At $\lambda = 1000$ nm, $T_D \approx 50$ %. Based on the observed trend, the T_D of light for $\lambda > 600$ nm could be further increased by increasing the texture height or periodicity. However, to conclude, an extended sample set is required. The scattering trend of short-wavelength light in this graph stands out as it does not show a direct relation with hexagonal feature sizes. This is explored further.

T_D of hexagonal textured wafers is plotted against the height of the saddle region in Fig. 10. The value $H_r - H_g$ represents the height of the saddle region. The graph includes T_D values in % for λ at 300 nm, 400 nm, 600 nm, 800 nm, 1000 nm and 1200 nm for 75 glass wafers. The solid lines are meant to guide the eye. Overall, T_D increases with the increase of $H_r - H_g$. However, the rate of increase differs with the
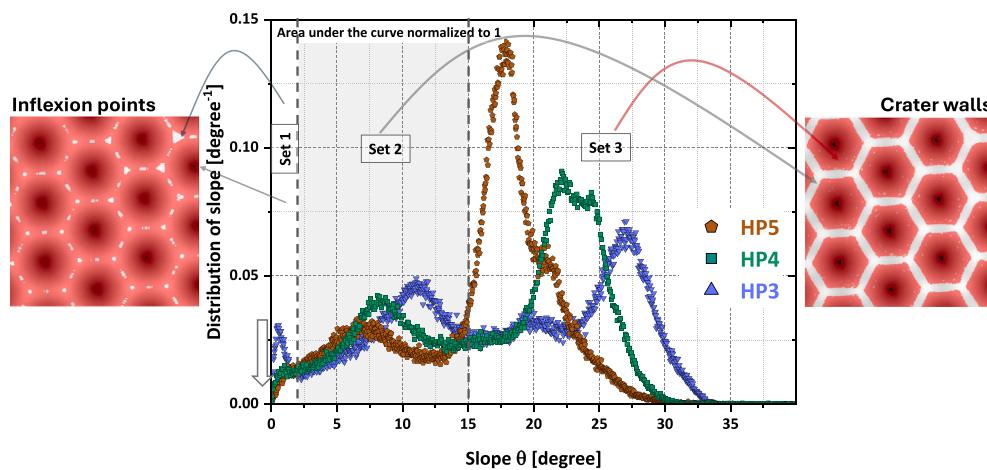

Fig. 7. Surface normal distribution curves of HP3, HP4 and HP5 in terms of angles. The occurrence value is normalised such that the total for each curve adds up to 1. Arrows mark different angle sets - HP5 is used for demonstration purposes. A detailed contribution of surface morphology to the angles is provided in the Supplementary Fig. 1.
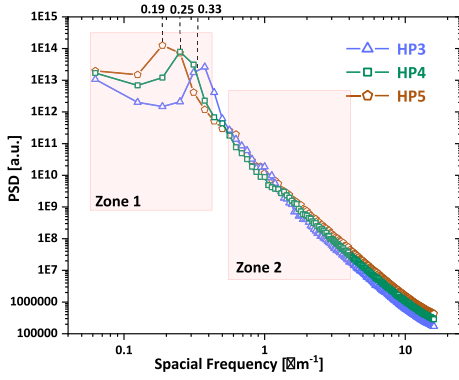
Fig. 8. PSD curves of HP3, HP4,and HP5 hexagonal microtextures. The reciprocal values of periodicity, i.e, 1/3, 1/4 and 1/5 are marked on the horizontal axis.

Fig. 10. Diffused transmission of different λ versus $H_r - H_g$ values of 3 μm, 4 μm and 5 μm hexagonal micro textures (75 samples). The lines in the image are guides to the eye.

λ of light. For $\lambda < 600$ nm, there is a rapid increase in scattering. For $\lambda = 300$ nm, T_D steeply rises and saturates around $H_r - H_g = 70$ nm and $\lambda = 400$ nm saturates at around 120 nm $H_r - H_g$. For $\lambda = 600$ nm, T_D shows a monotonic increase. For $\lambda > 600$ nm, the rate of increase in T_D is mild. This suggests that the influence of small feature heights is not significant in interactions with $\lambda > 600$ nm, implying that the scattering mechanism is not the same across the entire wavelength range considered. Most likely, the interaction with small features in the morphology is diffractive for $\lambda < 600$ nm, and these features do not significantly impact T_D beyond $\lambda = 600$ nm. As observed previously, texture height and periodicity play a primary role in scattering light with $\lambda > 600$ nm, which is likely to exhibit refractive scattering.

Fig. 11(A) shows the T_{TOT} and T_D spectra corresponding to the HC textures HP3, HP4 and HP5. Corresponding values of flat glass are also added as a reference (the T_D of flat glass is almost zero). T_{TOT} spectra show an anti-reflective nature of HC textures. An increase in transmission compared to flat glass is attributed to the angles formed by craters at the glass-air interface [46]. This property is well known for opaque hexagonal textures on wafer substrates with hexagonal holes facing illumination in concave mode [47–50]. It is worth noting that, in our study, the craters are positioned in a convex mode relative to the incident light as illustrated in Fig. 11(B). T_{TOT} rises with an increase in periodicity and AR. This is correlated with the θ_s of the hexagonal textures, specifically
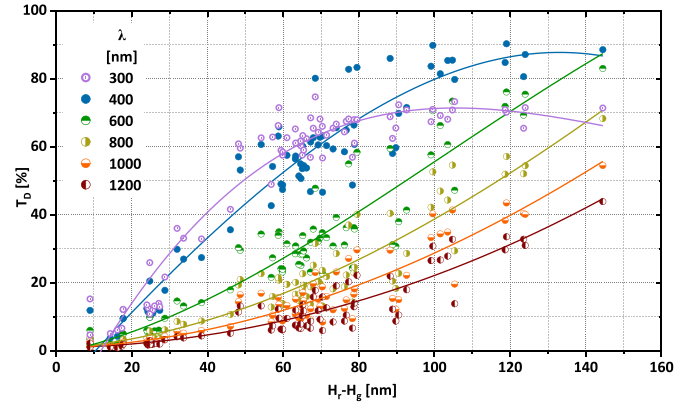
Set 3, which represents the surface angles of crater walls ($\theta_s > 15°$). The uniform taper on the gratings results in a gradual optical density variation [51], which results in reduced reflection at the interface [52]. Additionally, a high total contribution of HP5 in Set 3, combined with its crater height, results in multiple reflections within the glass medium, enhancing its T_{TOT}. The T_D spectra of HP5 are the highest, followed by HP4 and HP3, as already observed in Fig. 9.

3.2.2. Diffraction patterns made by hexagonal microtextures

The glass wafer, tessellated with periodic craters featuring hexagonal edges, can be considered a 2D hexagonal grating in transmission mode, where the 2D periodicity determines the diffraction pattern [53]. When light is incident on the flat side of the glass wafer, each hexagonal microscale crater can act as a plano-concave lens. The hexagonal shape ensures six-fold symmetry in both near- and far-field patterns, with the near-field exhibiting multiple HC shapes and the far-field showing a reciprocal lattice [53,54]. A near-field diffraction pattern at 3 μm (simulated using the angular spectrum method) and far-field diffraction at a 10 cm distance (simulated with fast Fourier transforms) are provided in Supplementary Fig. 6. To observe the far-field pattern in the real world, the flat side was probed with a 635 nm collimated diode laser. The hexagonal-shaped array creates a pattern with a central maximum
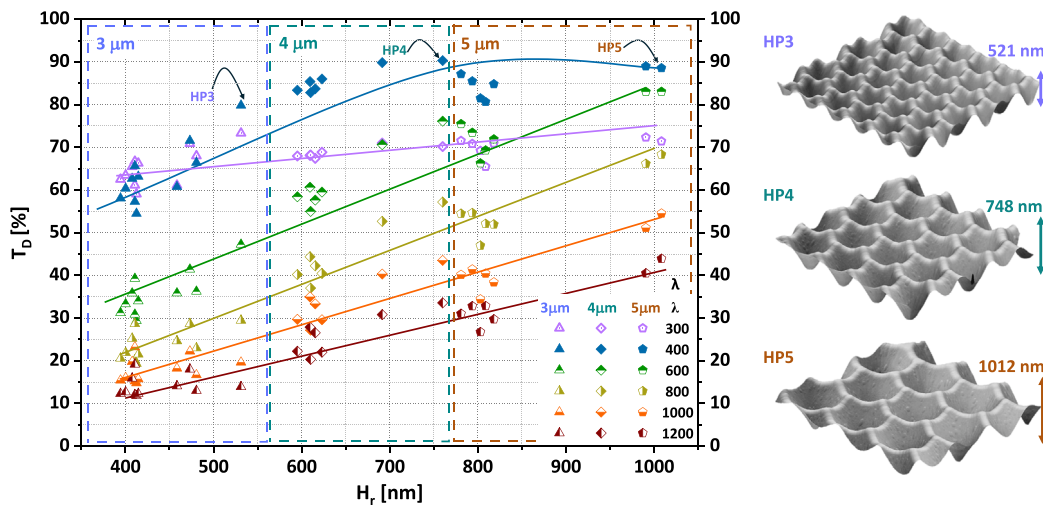

Fig. 9. Diffused transmission of different wavelengths versus profile height of 3 μm, 4 μm and 5 μm periodicity hexagonal micro textures (21 samples). The lines in the image are guides to the eye.
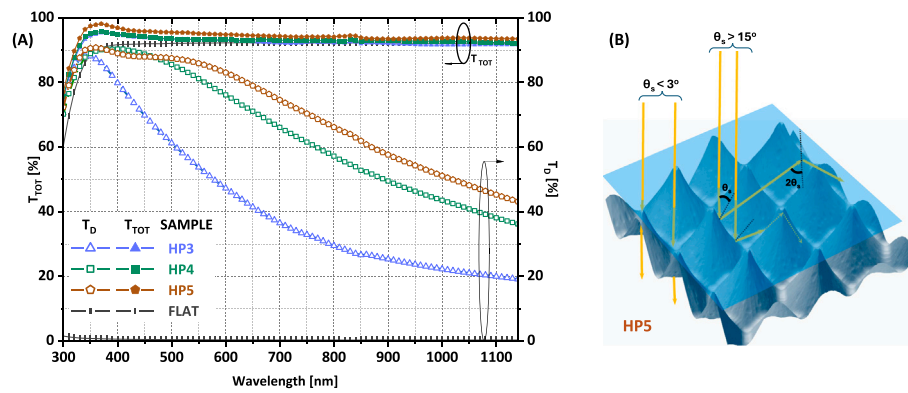
Fig. 11. (A) Total transmission spectra T_{TOT} and diffused transmission spectra T_D of hexagonal textured HP3, HP4, HP5 and non textured flat Corning glass wafers. (B) Illustration of the set of 3 angles of the crater, multiple reflections in the glass.
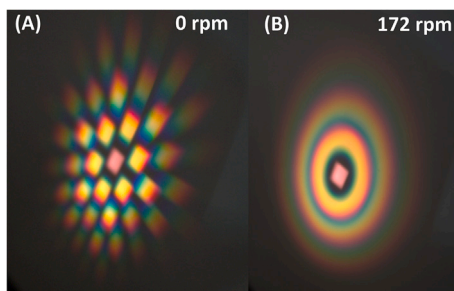

Fig. 12. (A) The far-field scattering of white light at 10 cm distance by hexagonal texture HP5. (B) Rings formed at the same distance with samples given 172 rpm. (For interpretation of the references to colour in this figure legend, the reader is referred to the web version of this article.)

(zeroth-order) of the highest intensity. A hexagonal array of bright light spots surrounds this central spot. The pattern is consistent with the theoretically simulated far-field pattern shown in the supplementary material. Additionally, the maxima surrounding the central peak are followed by weaker subsidiary maxima. The experimentally measured angular scattering intensity of white light by hexagonal textures is discussed in the following section.

3.2.3. AID of hexagonal microtextures

Far-field diffracted white light transmitted through HC patterns on glass, at a distance of 10 cm from the sample, is shown in Fig. 12(A). The diffracted orders, except for the central (zeroth) spot, will be coloured, as the light is dispersed into different wavelengths at various angles. To measure the angular scattering caused by the sample, the wafer was rotated at a speed of 172 rpm (as explained in Section 2.4). Coloured, discrete rings, as shown in Fig. 12(B), are formed at the detector plane.

The Fig. 13 shows the intensity distribution of the transmitted light versus transmission angles. Intensity for $\lambda = 300, 400, 600, 800$ and 1000 nm for HP3, HP4 and HP5 yields the following observations. (i) Among the plotted wavelengths, the specular component is the highest for $\lambda =1000$ nm (near 0° transmission angle), which agrees with the T_D in Fig. 11. This minor prominence of long wavelengths causes the central spot to appear red in Fig. 12(B). (ii) The subsequent orders depict the influence of wavelengths on scattered angles. For each set of maxima, the light is scattered at wider angles for longer wavelengths, due to which the patterns in Fig. 12(A) and (B) have coloured spots/rings in blue-to-red order in a radial outward direction. (iii) The amplitude of the first, second and subsequent orders in the AID plots is highest for HP5, followed by HP4 and HP3. The intensity redistribution due to

texture becomes most pronounced with increasing periodicity. (iv) The scattering pattern (as well as the rings used for the measurements here) becomes well defined with distinct peaks and zero intensity points with an increase in wavelength and periodicity. To summarise, the far-field diffraction pattern consists of hexagonally arranged diffraction spots, whose intensities are determined by the size and shape of the hexagonal microtexture.

3.3. Solar cells on honeycomb textures

Fig. 14 presents the external solar cell parameters of nc-Si:H single-junctions plotted as a function of AR for the different periodicities. The $J_{sc,EQE}$ increases directly with AR. This is a result of an increase in diffused transmission with total texture height and nanofeatures, as discussed in Section 3.2.1. It is also evident that the $J_{sc,EQE}$ increases with periodicity. This can be explained from the discussion in Section 3.2.2 that an increase in periodicity results in stronger diffraction and amplitudes over broad angles, which enhance light absorption through higher order diffraction channels [55]. The open-circuit voltage (V_{oc}) of the samples is independent of AR and the periodicity of the texture. The fill factor is significantly low for samples with small AR with 3 μm periodicity. This is a consequence of the steep walls of 3 μm periodic craters, contributing to shunt formation in silicon [56]. The solar cells exhibit similar fill factors for cells fabricated on 4 μm and 5 μm-periodic textures. A similar observation of near-constant electrical properties has been previously reported for single-junction cells fabricated on a hexagonal substrate configuration by Sai et al. [25].

The efficiency of the solar cells increases with AR as a combined effect of $J_{sc,EQE}$ and fill factor increase, reaching as high as 9.3 % at AR = 0.21 for the HP5. Based on trends in $J_{sc,EQE}$ and FF, the conversion efficiency could be further improved by increasing the AR and the periodicity. However, to draw a conclusive observation, an extensive sample set is required.

The sections below discuss the solar cells with the highest short-circuit current density and conversion efficiency for each periodicity. Hereafter, the nc-Si:H single-junction solar cells fabricated on flat glass, HP3, HP4 and HP5 will be referred to as FLAT, NHP3, NHP4 and NHP5, respectively. All solar cell parameters of FLAT, NHP3, NHP4 and NHP5 are tabulated and recorded in Table 2. In Fig. 15(A), the J-V curve of the 3.2 μm thick FLAT, NHP3, NHP4 and NHP5 nc-Si:H solar cells is plotted. The fill factor (FF) of the cells increases with periodicity. The low FF on FLAT is due to the low parallel resistances caused by crack formation in nc-Si:H absorber materials when deposited on flat surfaces [57]. The sheet resistance values of HP3, HP4, and HP5 show a subtle decrease with increasing periodicity, which can be speculated to be related to the steepness of the hexagons as discussed in Fig. 7.
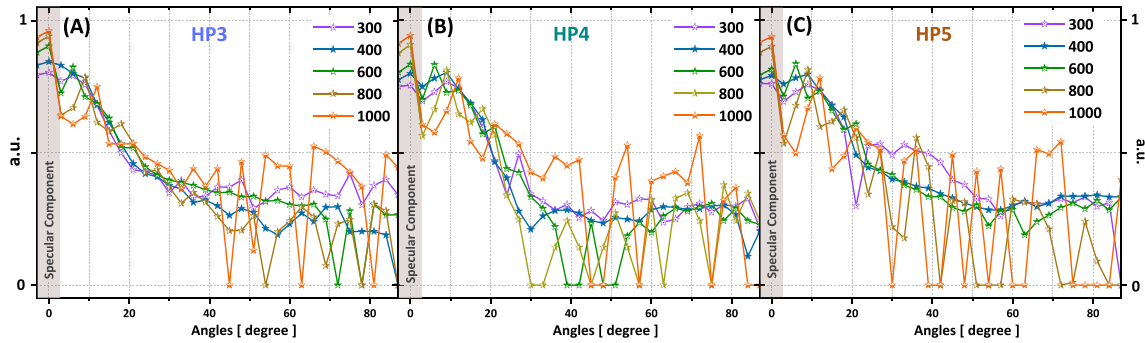
Fig. 13. Normalised Angular intensity distribution of hexagonal textures on glass for (a) HP3, (b) HP4 and (c) HP5.
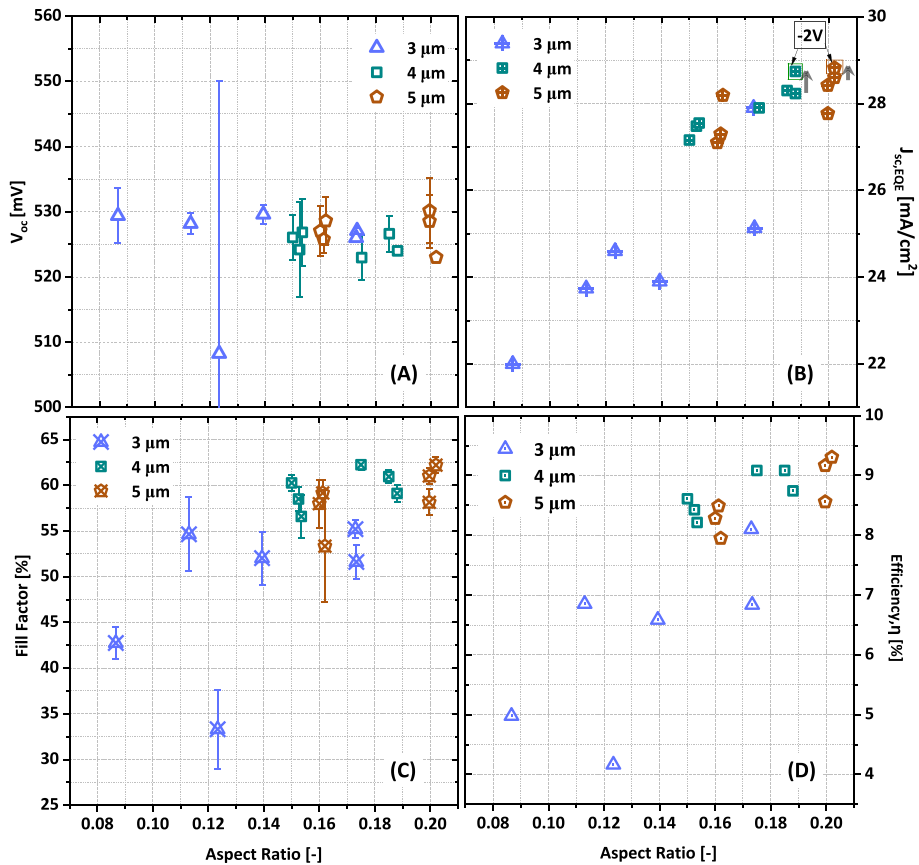

Fig. 14. The current-voltage parameters of 3200 nm (approximately) thick nc-Si:H single junction solar cells on superstrate configuration fabricated on hexagonal microtextures. The parameters (A) V_{oc}, (B) $J_{sc,EQE}$ (values marked using the box are measured at a reverse bias of 2V), (C) fill factor and (D) efficiency are plotted as a function of AR for different periodicities.

The steeper the walls, the greater the shadowing effect that can result in thin or non-uniform regions of the TCO layer, increasing the sheet resistance. The FF reported for NHP5 in this paper is typical for superstrate configuration (p-i-n) nc-Si:H single-junction solar cells with an absorber thickness of approximately 3200 nm and a thin TCO front electrode [7,58–61]. However, Tan et al. have reported 69 % FF for superstrate configuration on random microtextured glass with ZnO:Al front TCO for a similar absorber thickness [7]. This suggests a possibility for increasing the fill factor by increasing free carrier concentration in TCO [62] or increasing TCO thickness. An illustration of small-area solar cells distributed over glass substrates studied in this paper is shown in Supplementary Fig. 7 of this paper. A further enhancement in series resistance can also be achieved by reducing the distance between the front contact and the cells. A summary of the reported highest fill factors and open-circuit voltages of thin-film silicon solar cells with different cell architectures is included in Supplementary Fig. 4 of this paper.

3.3.1. Photocurrent density

Fig. 15(B) gives the measured EQE spectra of NHP3, NHP4 and NHP5. The highest short-circuit current density of 28.6 mA/cm^2 is achieved on NHP5 (H_r = 1012 nm and AR = 20.2 %). To the best of the author's knowledge, this is the highest reported $J_{sc,EQE}$ for p-i-n superstrate silicon solar cells without external anti-reflection coating (Supplementary Fig. 3). This is an increase of 24 % $J_{sc,EQE}$ in reference compared to FLAT. NHP5 is followed by NHP4 with $J_{sc,EQE}$ = 28.2 mA/cm^2 (H_r = 748 nm and AR = 18.8 %) and NHP3 with $J_{sc,EQE}$ = 27.9 mA/cm^2 (H_r = 521 nm and AR = 17.3 %).

Table 2
Solar cell parameters for nc-Si:H single-junction solar cells on textures of different periodicities. The standard deviation (σ_d) for electrical performance parameters is calculated based on the 5 best-performing cells of each substrate. $\sigma_d(V_{oc}) \approx 3$ mV, $\sigma_d(FF) \approx 0.7$ %, $\sigma_d(R_s) \approx 0.1$ Ω.m^2, $\sigma_d(R_p) \approx 0.1$ kΩ.m^2. R_{sheet} is calculated based on 8 measurements on 150-nm thick IOH deposited over glass. $\sigma_d(R_{sheet,IOH}) \approx 0.7$ Ω/sq.

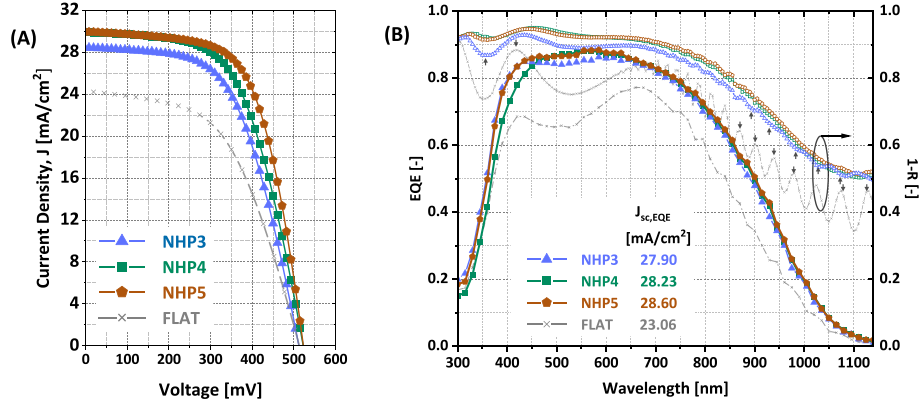| Sample	**P** [μm]	$R_{sheet,IOH}$ [Ω/sq]	$J_{sc,EQE}$ [mA/cm^2]	V_{oc} [mV]	FF [%]	R_s [Ω.cm^2]	R_p [kΩ.cm^2]	**Eff** [%]
FLAT	0	21	23.0	511	55.0	19.4	0.9	6.5
NHP3	3	25	27.9	526	55.2	18.1	1.9	8.1
NHP4	4	23	28.2	524	59.1	12.9	2.1	8.7
NHP5	5	22	28.6	523	62.2	9.6	1.9	9.3

Fig. 15. (A) EQE spectra and (B) Current density versus voltage (J-V) characteristics of nc-Si:H single junction solar cells NHP3, NHP4, NHP5 fabricated on hexagonal microtextures with periodicity 3 μm (HP3), 4 μm (HP4) and 5 μm (HP5) respectively. An nc-Si:H single-junction solar cell fabricated on FLAT is added for reference. All absorber nc-Si:H layers are 3200 nm thick. Arrows mark the $1 - R$ peaks due to Fabry-Perot interference.

Over the entire spectrum, the total absorption ($1 - R$) of the solar cell increases with increasing periodicity of the glass as a result of uniform tapering as previously reported by Chutinan et al. [51] and Sai et al. [52]. This additional transmission is directly translated to the EQE spectra of NHP5 when compared to NHP3 and NHP4. The high $J_{sc,EQE}$ observed in the hexagonal microtextures when compared to flat glass arises from a combined effect of the anti-reflective nature and enhanced light trapping in the solar cells. A similar discussion has been reported previously by Chong et al. correlating the rise in $J_{sc,EQE}$ to gratings on the illuminated surface of the solar cell [48]. These surface gratings can diffract light into multiple orders, trapping it within the absorbing layer [11,45]. Although the $1 - R$ spectra of NHP5 and NHP4 are very similar, NHP4 shows a lower blue response than NHP5. This difference may arise from parasitic absorption in the (p)nc-SiO$_x$:H layer of the solar cell due to unexpected variations in processing conditions.

Hexagonal microtextured superstrate glass significantly increases the EQE in the long-wavelength region compared to FLAT. This can be attributed to the high T_D exhibited by HC textures in transmission (Section 3.2). The hexagonal texture with sufficient H_r is capable of quenching Fabry-Perot interference in the nc-Si:H absorber in the near-IR region when compared with FLAT (marked by downward arrows in Fig. 15(B)). Interference fringes with diminished amplitudes appear in the $1 - R$ of the NHP3 cell (marked by upward arrows) and some other solar cells fabricated on low AR wafers with 3 μm periodicity (not shown in this paper). This is speculated to be due to the less deep craters of the 3 μm periodic textures when compared to other considered periodicities (refer to Fig. 9).

The high values in the near-IR response are also due to the silver back reflector, which adapts to the hexagonal morphology, combined with the natural texture of the nanocrystalline material. Fig. 16(A) and (B) are the AFM scans and (C) and (D) are the SEM images representing before

and after deposition of silicon layers on HP5 from the non-illuminated side of the absorber layer. In a PECVD-deposited thin-film silicon solar cell, the surface morphology is conventionally not externally guided but instead naturally formed through crystal growth. This flattens out the textures and reduces their amplitude [31]. Although the amplitudes and sharpness of the hexagons decrease when a 3200 nm thick silicon film is deposited, as evident from Figs. 16(B) and (D), the surface still resembles distinct hexagonal shapes. This suggests that the back reflector Ag layer forms an HC morphology with a height of 916 nm (AR = 0.14 and an RMS roughness of 278 nm). These Ag back reflectors with HC morphology are similar to back reflectors employed in thin-film silicon cells in substrate configurations, which are well known for enhancing near-IR responses [19,27,31].

3.3.2. nc-Si:H film growth

To inspect the growth of the nc-Si film on hexagonal microtextures, an SEM image of NHP4 is shown in Fig. 17. The nc-Si growth appears to be conformal. The nc-Si absorber deposited on the hexagonal microtexture is of high quality with minimal defects. A crack is observed near the back contact in the bulk, away from the glass, which is highlighted and zoomed in. These kinds of defects can cause a drop in parallel resistance (R_p) and, in turn, a decrease in FF in the solar cells, as observed in the cells presented in this paper. Silicon crystals, when deposited on hexagonal textures, have been reported to develop cracks in the vicinity of an imaginary focal point of the curve due to shadowing effects [16,28]. However, a 4.4 μm thick nc-Si:H ($\chi_c \approx 60\%$) deposited on HP4 does not demonstrate any cracks of this type in the absorber bulk (HP4 yields a focal distance of 3.3 μm as depicted in Supplementary Fig. 5). Hexagonal microtextures on glass with considered periodicity - AR combination can facilitate the formation of high-quality nc-Si:H filaments, eliminating shadowing effects.
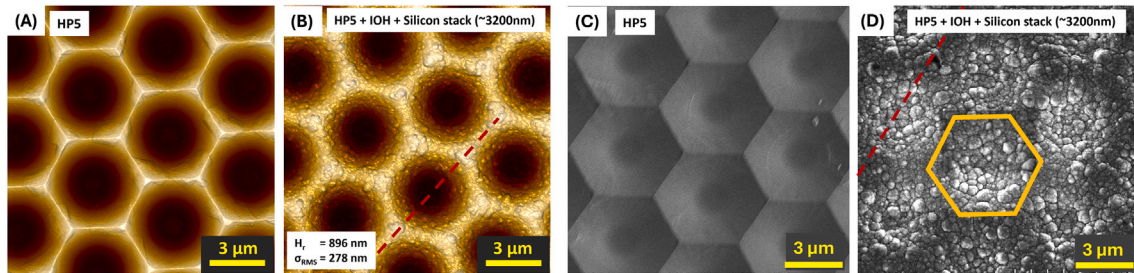
Fig. 16. nc-Si:H single junction solar cell characterised from the n-layer side before depositing the silver back reflector and back contact. (A) AFM and (B) SEM of bare textured glass (period = 4 μm). (C) AFM and (D) SEM of solar cell absorber after depositing IOH (150 nm)/(p)nc-SiO$_x$:H (16 nm)/(i)nc-Si:H (3200 nm)/(n)nc-SiO$_x$:H (20 nm). (For interpretation of the references to colour in this figure legend, the reader is referred to the web version of this article.)
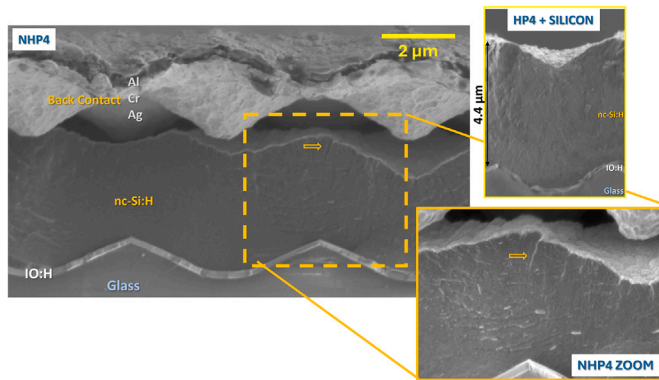

Fig. 17. SEM cross-sectional image of a 3.2 μm thick nc-Si:H cell on a 4 μm period hexagonal microtextured glass superstrate.

4. Conclusion

This paper reports hexagonal microtextures on glass, their optical properties and their application in nc-Si:H solar cell devices. The surface morphology and optical properties of the textures are reported. Features of multiple size ranges characterise the HC surface morphology. Hexagonal textures exhibit enhanced light transmission across all wavelengths, with an increase in periodicity. Hexagonal textures exhibit enhanced light transmission across the entire wavelength range when the periodicity is increased. Hexagonal textures with deeper craters also display high diffused transmission and broad-angle scattering properties. These properties directly translate to EQE spectra of solar cells fabricated on the textures, increasing the photoresponse and efficiency with an increase in periodicity and aspect ratio of the hexagonal microtextures. Hexagonal textures with a 5 μm periodicity with a 20.2 % AR yield a photocurrent of 28.6 mA/cm^2 and a photo conversion efficiency of 9.30 %. It is also observed that the HC textures in the superstrate configuration glass can facilitate high V_{oc} and crack-free nc-Si:H crystal growth. This indicates a high potential for hexagonal textures on glass in multijunction thin-film solar cell applications.

CRediT authorship contribution statement

Govind Padmakumar: Writing – original draft, Visualization, Validation, Methodology, Formal analysis, Data curation, Conceptualization. **Aravind Balaji:** Visualization, Resources. **Federica Saitta:** Resources. **Paula Perez-Rodriguez:** Writing – review & editing, Supervision. **René A.C.M.M. van Swaaij:** Writing – review & editing. **Arno H.M. Smets:** Writing – review & editing, Supervision, Project administration, Funding acquisition, Conceptualization.

Declaration of competing interests

The authors declare the following financial interests/personal relationships that may be considered potential competing interests:

Appendix A. Supplementary data

Supplementary data for this article can be found online at doi:10.1016/j.solener.2025.114292.

Data availability

Data will be made available on request.

References

[1] K. Jäger, U. Aeberhard, E. Alarcon Llado, B. Bläsi, S. Burger, B. Ehrler, W. Favre, A. Fejfar, T. Gageot, I. Gordon, H. Helmers, O. Höhn, O. Isabella, M. Jošt, M. Ledinský, J. Mandal, P. Manley, D. Muñoz, Z. Omair, J.C. Ortiz Lizcano, U.W. Paetzold, A.P. Raman, H. Sai, R. Saive, M. Schmid, E. Yablonovitch, C. Becker, Optics for Terawatt-scale photovoltaics: review and perspectives, Adv. Opt. Photon. 17 (1) (2025) 185, https://doi.org/10.1364/AOP.530556
[2] E. Yablonovitch, Statistical Ray Optics, Tech. Rep. 7, 1982.
[3] J. Zhao, A. Wang, M.A. Green, F. Ferrazza, 19.8% efficient "honeycomb" textured multicrystalline and 24.4% monocrystalline silicon solar cells, Appl. Phys. Lett. 73 (14) (1998) 1991–1993, https://doi.org/10.1063/1.122345
[4] J. Zhao, A. Wang, P. Campbell, M.A. Green, A 19.8% Efficient Honeycomb Multicrystalline Silicon Solar Cell with Improved Light Trapping, Tech. Rep. 10, 1999.
[5] C. Battaglia, C.M. Hsu, K. Söderström, J. Escarré, F.J. Haug, M. Charrière, M. Boccard, M. Despeisse, D.T.L. Alexander, M. Cantoni, Y. Cui, C. Ballif, Light trapping in solar cells: can periodic beat random? ACS Nano 6 (3) (2012) 2790–2797, https://doi.org/10.1021/nn300287j
[6] H. Tan, E. Moulin, F.T. Si, J.-W. Schüttauf, M. Stuckelberger, O. Isabella, F.-J. Haug, C. Ballif, M. Zeman, A.H.M. Smets, Highly transparent modulated surface textured front electrodes for high-efficiency multijunction thin-film silicon solar cells, Prog. Photovolt.: Res. Appl. 23 (8) (2015) 949–963, https://doi.org/10.1002/pip.2639
[7] H. Tan, E. Psomadaki, O. Isabella, M. Fischer, P. Babal, R. Vasudevan, M. Zeman, A.H.M. Smets, Micro-textures for efficient light trapping and improved electrical performance in thin-film nanocrystalline silicon solar cells, Appl. Phys. Lett. 103 (17) (2013) 173905, https://doi.org/10.1063/1.4826639
[8] G. Yang, R.A. van Swaaij, H. Tan, O. Isabella, M. Zeman, Modulated surface textured glass as substrate for high performing microcrystalline silicon solar cells, Sol. Energy Mater. Sol. Cells 133 (2015) 156–162, https://doi.org/10.1016/j.solmat.2014.11.013
[9] G. Yang, R.A.C.M.M. van Swaaij, O. Isabella, M. Zeman, A novel way of texturing glass for microcrystalline silicon thin film solar cells application, Prog. Photovolt. Res. Appl. 23 (10) (2015) 1283–1290, https://doi.org/10.1002/pip.2550
[10] F.J. Haug, A. Naqavi, C. Ballif, Diffraction and absorption enhancement from textured back reflectors of thin film solar cells, J. Appl. Phys. 112 (2) (Jul 2012), https://doi.org/10.1063/1.4737606
[11] F.J. Haug, K. Söderström, A. Naqavi, C. Ballif, Resonances and absorption enhancement in thin film silicon solar cells with periodic interface texture, J. Appl. Phys. 109 (8) (Apr 2011), https://doi.org/10.1063/1.3569689

[12] K. Söderström, F.J. Haug, J. Escarŕ, O. Cubero, C. Ballif, Photocurrent increase in n-i-p thin film silicon solar cells by guided mode excitation via grating coupler, Appl. Phys. Lett. 96 (21) (May 2010), https://doi.org/10.1063/1.3435481

[13] H. Sai, T. Matsui, K. Matsubara, M. Kondo, I. Yoshida, 11.0%-efficient thin-film microcrystalline silicon solar cells with honeycomb textured substrates, IEEE J. Photovolt. 4 (6) (2014) 1349–1353, https://doi.org/10.1109/JPHOTOV.2014.2355037

[14] S.Q. Hussain, A.H.T. Le, K. Mallem, H. Park, M. Ju, Y. Kim, J. Cho, J. Park, Y. Kim, J. Yi, Using the light scattering properties of multi-textured AZO films on inverted hemisphere textured glass surface morphologies to improve the efficiency of silicon thin film solar cells, Appl. Surf. Sci. 447 (2018) 866–875, https://doi.org/10.1016/j.apsusc.2018.03.143

[15] A. Micco, A. Ricciardi, M. Pisco, V. La Ferrara, L.V. Mercaldo, P. Delli Veneri, A. Cutolo, A. Cusano, Light trapping efficiency of periodic and quasiperiodic back-reflectors for thin film solar cells: a comparative study, J. Appl. Phys. 114 (6) (Aug 2013), https://doi.org/10.1063/1.4817914

[16] H. Sai, K. Saito, N. Hozuki, M. Kondo, Relationship between the cell thickness and the optimum period of textured back reflectors in thin-film microcrystalline silicon solar cells, Appl. Phys. Lett. 102 (5) (2013) 053509, https://doi.org/10.1063/1.4790642

[17] D.Y. Kim, R. Santbergen, K. Jäger, M. Sever, J. Krč, M. Topič, S. Hänni, C. Zhang, A. Heidt, M. Meier, R.A.C.M.M. Van Swaaij, M. Zeman, Effect of substrate morphology slope distributions on light scattering, nc-si:h film growth, and solar cell performance, ACS Appl. Mater. Interfaces 6 (24) (2014) 22061–22068, https://doi.org/10.1021/am5054114

[18] T.C. Hales, The honeycomb conjecture, Jun, 1999.

[19] T. De Vrijer, M. Wiering, D. Van Nijen, G. Padmakumar, S. Sambamurthy, G. Limodio, A.H.M. Smets, The optical performance of random and periodic textured mono crystalline silicon surfaces for photovoltaic applications, EPJ Photovolt. 13 (2022), https://doi.org/10.1051/epjpv/2022021

[20] D. Eisenhauer, H. Sai, T. Matsui, G. Köppel, B. Rech, C. Becker, Honeycomb micro-textures for light trapping in multi-crystalline silicon thin-film solar cells, Opt. Express 26 (10) (2018) A498, https://doi.org/10.1364/oe.26.00a498

[21] S.Y. Chou, P.R. Krauss, P.J. Renstrom, Nanoimprint lithography, J. Vac. Sci. Technol. B 14 (6) (1996) 4129–4133, https://doi.org/10.1116/1.588605

[22] R.E. Russo, X.L. Mao, J. Yoo, J.J. Gonzalez, Laser ablation, in: Laser-Induced Breakdown Spectroscopy, Elsevier, 2007, pp. 41–70, https://doi.org/10.1016/B978-0-12-818829-3.00003-4

[23] Y. Wang, C. Ke, T. Wu, X. Zhao, R. Wang, Nanosecond laser texturing with hexagonal honeycomb micro-structure on titanium for improved wettability and optical properties, Optik 192 (Sep 2019), https://doi.org/10.1016/j.ijleo.2019.162953

[24] W.M. Moreau, Semiconductor Lithography, Springer US, Boston, MA, 1988, https://doi.org/10.1007/978-1-4613-0885-0

[25] H. Sai, K. Saito, M. Kondo, Investigation of textured back reflectors with periodic honeycomb patterns in thin-film silicon solar cells for improved photovoltaic performance, IEEE J. Photovolt. 3 (1) (2013) 5–10, https://doi.org/10.1109/JPHOTOV.2012.2213800

[26] Y. Saito, T. Kosuge, Honeycomb-textured structures on crystalline silicon surfaces for solar cells by spontaneous dry etching with chlorine trifluoride gas, Sol. Energy Mater. Sol. Cells 91 (19) (2007) 1800–1804, https://doi.org/10.1016/j.solmat.2007.06.009

[27] H. Sai, T. Matsui, A. Bidiville, T. Koida, Y. Yoshida, K. Saito, M. Kondo, Light Management Using Periodic Textures for Enhancing Photocurrent and Conversion Efficiency in Thin-Film Silicon Solar Cells, Tech. rep., 2013.

[28] T. Matsui, H. Sai, A. Bidiville, H.-J. Hsu, K. Matsubara, Progress and limitations of thin-film silicon solar cells, Solar Energy 170 (May) (2018) 486–498, https://doi.org/10.1016/j.solener.2018.05.077

[29] H. Sai, T. Matsui, K. Saito, M. Kondo, I. Yoshida, Photocurrent enhancement in thin-film silicon solar cells by combination of anti-reflective sub-wavelength structures and light-trapping textures, Prog. Photovolt. Res. Appl. 23 (11) (2015) 1572–1580, https://doi.org/10.1002/pip.2594

[30] H. Sai, T. Matsui, K. Matsubara, Stabilized 14.0%-efficient triple-junction thin-film silicon solar cell, Appl. Phys. Lett. 109 (18) (2016) 183506, https://doi.org/10.1063/1.4966996

[31] H. Sai, K. Saito, M. Kondo, Enhanced photocurrent and conversion efficiency in thin-film microcrystalline silicon solar cells using periodically textured back reflectors with hexagonal dimple arrays, Appl. Phys. Lett. 101 (17) (2012) 173901, https://doi.org/10.1063/1.4761956

[32] K. Jäger, O. Isabella, L. Zhao, M. Zeman, Light scattering properties of surface-textured substrates, Phys. Status Solidi C 7 (3–4) (2010) 945–948, https://doi.org/10.1002/pssc.200982695

[33] G. Padmakumar, A. Balaji, M. Criel, F. Saitta, G. Limodio, P. Perez Rodriguez, R.A.C.M.M. Van Swaaij, A.H.M. Smets, Engineering of hexagonal microtextures on glass, ACS Appl. Opt. Mater. 3 (10) (Oct 2025), https://doi.org/10.1021/acsaom.5c00328

[34] H. Park, J.H. Cho, J.H. Jung, P.P. Duy, A.H.T. Le, J. Yi, A review of wet chemical etching of glasses in hydrofluoric acid based solution for thin film silicon solar cell application (1), Curr. Photovolt. Res. (3) (2017) 75–82.

[35] Corning Incorporated, Semiconductor Glass Wafers Product Information Sheet, Tech. rep., 2015.

[36] Corning Incorporated, Exceptional Dimensional Stability and Surface Quality in Thin, Large-Size Sheets, Tech. rep., 2021, www.corning.com/worldwide/en/products/display-glass.html.

[37] A.H.M. Smets, Growth Related Material Properties of Hydrogenated Amorphous Silicon, Technische Universiteit Eindhoven, 2002, https://doi.org/10.6100/IR556557

[38] J.M. Bennett, L. Mattsson, Introduction to Surface Roughness and Scattering, Optical Society of America, 1989, https://doi.org/10.1364/1557521085

[39] O. Isabella, J. Krč, M. Zeman, Modulated surface textures for enhanced light trapping in thin-film silicon solar cells, Appl. Phys. Lett. 97 (10) (2010) 101106, https://doi.org/10.1063/1.3488023

[40] K. Jäger, O. Isabella, R.A.C.M.M. van Swaaij, M. Zeman, Angular resolved scattering measurements of nano-textured substrates in a broad wavelength range, Meas. Sci. Technol. 22 (10) (2011) 105601, https://doi.org/10.1088/0957-0233/22/10/105601

[41] H. Scherg-Kurmes, S. Seeger, S. Körner, B. Rech, R. Schlatmann, B. Szyszka, Optimization of the post-deposition annealing process of high-mobility in2o3:h for photovoltaic applications, Thin Solid Films 599 (2016) 78–83, https://doi.org/10.1016/j.tsf.2015.12.054

[42] C. Battaglia, L. Erni, M. Boccard, L. Barraud, J. Escarré, K. Sderstrm, G. Bugnon, A. Billet, L. Ding, M. Despeisse, F.J. Haug, S. Wolf de, C. Ballif, Micromorph thin-film silicon solar cells with transparent high-mobility hydrogenated indium oxide front electrodes, J. Appl. Phys. 109 (11) (Jun 2011), https://doi.org/10.1063/1.3592885

[43] S. Olibet, C. Monachon, A. Hessler-Wyser, E. Vallat-Sauvain, S. De Wolf, L. Fesquet, J. Damon-Lacoste, C. Ballif, Textured silicon heterojunction solar cells with over 700mv open circuit voltage studied by transmission electron microscopy, Tech. rep.

[44] C. Kothandaraman, T. Tonon, C. Huang, A.E. Delahoy, Improvement of a-si:h p-i-n devices using zinc oxide-based back-reflectors, Tech. rep.

[45] K. Jäger, G. Köppel, M. Hammerschmidt, S. Burger, C. Becker, On accurate simulations of thin-film solar cells with a thick glass superstrate, Opt. Express 26 (2) (2018) A99, https://doi.org/10.1364/oe.26.000a99

[46] H.K. Raut, V.A. Ganesh, A.S. Nair, S. Ramakrishna, Anti-reflective coatings: a critical, in-depth review, Energy Environ. Sci. (10) (2011), https://doi.org/10.1039/c1ee01297e

[47] E. Manea, E. Budianu, M. Purica, I. Cernica, F. Babarada, Technological process for a new silicon solar cell structure with honeycomb textured front surface, Sol. Energy Mater. Sol. Cells 90 (15) (2006) 2312–2318, https://doi.org/10.1016/j.solmat.2006.03.036

[48] T.K. Chong, J. Wilson, S. Mokkapati, K.R. Catchpole, Optimal wavelength scale diffraction gratings for light trapping in solar cells, J. Opt. 14 (2) (2012), https://doi.org/10.1088/2040-8978/14/2/024012

[49] C. Haase, H. Stiebig, Thin-film silicon solar cells with efficient periodic light trapping texture, Appl. Phys. Lett. 91 (6) (2007), https://doi.org/10.1063/1.2768882

[50] B. Yang, M. Lee, Fabrication of honeycomb texture on poly-si by laser interference and chemical etching, Appl. Surf. Sci. 284 (2013) 565–568, https://doi.org/10.1016/j.apsusc.2013.07.134

[51] A. Chutinan, N.P. Kherani, S. Zukotynski, High-efficiency photonic crystal solar cell architecture, Opt. Express 17 (11) (2009) 8871, https://doi.org/10.1364/OE.17.008871

[52] H. Sai, H. Fujii, K. Arafune, Y. Ohshita, Y. Kanamori, H. Yugami, M. Yamaguchi, Wide-angle antireflection effect of subwavelength structures for solar cells, Jpn. J. Appl. Phys, Part 1: Regul. Pap. Short Notes Rev. Pap. 46 (6 A) (2007) 3333–3336, https://doi.org/10.1143/JJAP.46.3333

[53] Hecht Eugene, Optics, fourth ed, Addison Wesley, San Francisco, CA 94111, 2002.

[54] J.W. Goodman, Introduction to Fourier Optics, fourth ed, W. H. Freeman and Company, New York, NY 10004-1562, 2017.

[55] H. Sai, Y. Kanamori, K. Arafune, Y. Ohshita, M. Yamaguchi, Light trapping effect of submicron surface textures in crystalline SI solar cells, Prog. Photovolt. Res. Appl. 15 (5) (2007) 415–423, https://doi.org/10.1002/pip.754

[56] D.Y. Kim, S. Hänni, J.W. Schüttauf, R.A.C.M.M. Van Swaaij, M. Zeman, Quantification of valleys of randomly textured substrates as a function of opening angle: correlation to the defect density in intrinsic nc-si:h, ACS Appl. Mater. Interfaces 8 (32) (2016) 20660–20666, https://doi.org/10.1021/acsami.6b03995

[57] E. Vallat-Sauvain, J. Bailat, J. Meier, X. Niquille, U. Kroll, A. Shah, Influence of the substrate's surface morphology and chemical nature on the nucleation and growth of microcrystalline silicon, Thin Solid Films 485 (1–2) (2005) 77–81, https://doi.org/10.1016/j.tsf.2005.03.017

[58] S. Klein, F. Finger, R. Carius, M. Stutzmann, Deposition of microcrystalline silicon prepared by hot-wire chemical-vapor deposition: the influence of the deposition parameters on the material properties and solar cell performance, J. Appl. Phys. 98 (2) (2005) 024905, https://doi.org/10.1063/1.1957128

[59] O. Vetterl, A. Lambertz, A. Dasgupta, F. Finger, B. Rech, O. Kluth, H. Wagner, Thickness dependence of microcrystalline silicon solar cell properties, Sol. Energy Mater. Sol. Cells 66 (1–4) (2001) 345–351, https://doi.org/10.1016/S0927-0248(00)00193-8

[60] H. Sai, K. Maejima, T. Matsui, T. Koida, K. Matsubara, M. Kondo, Y. Takeuchi, S. Sugiyama, H. Katayama, I. Yoshida, Impact of front TCO layer in substrate-type thin-film microcrystalline silicon solar cells, in: 2015 IEEE 42nd Photovoltaic Specialist Conference (PVSC), IEEE, 2015, pp. 1–6, https://doi.org/10.1109/PVSC.2015.7355677

[61] T. de Vrijer, S. Miedema, T. Blackstone, D. van Nijen, C. Han, A.H.M. Smets, Application of metal, metal-oxide, and silicon-oxide based intermediate reflective layers for current matching in autonomous high-voltage multijunction photovoltaic devices, Prog. Photovolt.: Res. Appl. 30 (12) (2022) 1400–1409, https://doi.org/10.1002/pip.3600

[62] F. Saitta, G. Padmakumar, P.P. Rodriguez, A. Wilson, P. Gonugunta, P.R. Anusuyadevi, R. Santbergen, A.H.M. Smets, Room-temperature sputtered sno2-based thin films as earth-abundant transparent conductive oxides for photovoltaic applications, ACS Appl. Electron. Mater. 7 (20) (2025) 9489–9504, https://doi.org/10.1021/acsaelm.5c01650